Hα and Hβ Emission in a C3.3 Solar Flare: Comparison between Observations and Simulations

Vincenzo Capparelli[1], Francesca Zuccarello[1] , Paolo Romano[2] , Paulo J. A. Simões[3], Lyndsay Fletcher[3], David Kuridze[4] ,
Mihalis Mathioudakis[4] , Peter H. Keys[4], Gianna Cauzzi[5] , and Mats Carlsson[6]

[1] Dipartimento di Fisica e Astronomia—Sezione Astrofisica, Universitá di Catania, via S. Sofia 78, I-95123 Catania, Italy; vca@oact.inaf.it
[2] INAF—Osservatorio Astrofisico di Catania, via S. Sofia 78, I-95123 Catania, Italy
[3] SUPA, School of Physics & Astronomy, University of Glasgow, G12 8QQ, Scotland, UK
[4] Astrophysics Research Centre, School of Mathematics & Physics, Queen's University Belfast, Belfast BT7 1NN, UK
[5] INAF—Osservatorio Astrofisico di Arcetri, Largo E. Fermi 5, I-50125 Firenze, Italy
[6] Institute of Theoretical Astrophysics, University of Oslo, P.O. Box 1029 Blindern, NO-0315 Oslo, Norway
Received 2017 June 12; revised 2017 September 11; accepted 2017 October 3; published 2017 November 14

Abstract

The hydrogen Balmer series is a basic radiative loss channel from the flaring solar chromosphere. We report here on the analysis of an extremely rare set of simultaneous observations of a solar flare in the Hα and Hβ lines, at high spatial and temporal resolutions, that were acquired at the Dunn Solar Telescope. Images of the C3.3 flare (SOL2014-04-22T15:22) made at various wavelengths along the Hα line profile by the Interferometric Bidimensional Spectrometer (IBIS) and in the Hβ with the Rapid Oscillations in the Solar Atmosphere (ROSA) broadband imager are analyzed to obtain the intensity evolution. The Hα and Hβ intensity excesses in three identified flare footpoints are well-correlated in time. We examine the ratio of Hα to Hβ flare excess, which was proposed by previous authors as a possible diagnostic of the level of electron-beam energy input. In the stronger footpoints, the typical value of the the Hα/Hβ intensity ratio observed is ∼0.4–0.5, in broad agreement with values obtained from a RADYN non-LTE simulation driven by an electron beam with parameters constrained (as far as possible) by observation. The weaker footpoint has a larger Hα/Hβ ratio, again consistent with a RADYN simulation, but with a smaller energy flux. The Hα line profiles observed have a less prominent central reversal than is predicted by the RADYN results, but can be brought into agreement if the Hα-emitting material has a filling factor of around 0.2–0.3.

Key words: Sun: activity – Sun: chromosphere – Sun: flares – Sun: photosphere – techniques: high angular resolution

1. Introduction

Solar flares are explosive phenomena occurring in the solar atmosphere that indicate a rapid conversion of magnetic energy into other forms of energy (kinetic, radiative, particle acceleration, etc.). This process, which is believed to result from magnetic reconnection within a region with highly unstable magnetic field configurations, can produce electromagnetic radiation emission for almost the entire electromagnetic spectrum (depending on the energy involved, which can span from 10^{28} to 10^{32} erg), and is associated with an increase in brightness of the corona, chromosphere, and occasionally the photosphere (see, e.g., Fletcher et al. 2011 and references therein, for a review).

Several mechanisms are involved in such a broad range of electromagnetic radiation emission at various atmospheric heights. Flares are often contextualized in the well-known CSHKP flare geometry (named for Carmichael 1964; Sturrock 1966; Hirayama 1974 and Kopp & Pneuman 1976), which suggests that when an instability sets in, magnetic reconnection takes place (usually at the coronal level), resulting in electrons and protons being accelerated. But models dealing with coronal processes have little to say about the details of the generation of flare chromospheric emission,

particularly in the lower atmosphere. Initial models of atmospheric emission lines were based on empirical models of flaring atmospheres, or, assuming an electron-beam plasma heating mechanism, radiative transfer simulations (Canfield et al. 1984). However, more recently we have started to turn to radiation-hydrodynamic (RHD) flare simulations (Abbett & Hawley 1999; Allred et al. 2005 and Kašparová et al. 2009), which model the effect of accelerated particles traveling through the lower atmospheric layers, impulsively heating the local plasma, and causing an expansion of the chromosphere in a process termed chromospheric evaporation.

To test and constrain the electron-beam energy transport model, we need to identify sensitive diagnostic radiation signatures, observations of which can be compared to the output of targeted numerical simulations. In this regard, the chromosphere presents an ideal test-bed for analyzing the release and redistribution of energy from accelerated particles in this region. In particular, observation and modeling of spectral lines emergent from different layers of the chromosphere can be used to understand how the chromosphere responds to energy input at different heights, and thereby to constrain the beam properties. But such investigations also serve an additional, exploratory purpose by helping us to identify the best ways—e.g., choices of wavelength, and temporal and spectral resolutions—to get the maximum diagnostic power from flare optical observations, which can be very challenging to plan and execute.

In this paper we present flare observations at high temporal and spatial resolutions in the Hα and Hβ lines, with accompanying RHD simulations. Though they are among the strongest spectral lines emitted by flares, simultaneous observations in these two lines are very rare. This flare is therefore of interest, as we can probe the behavior of Hα and Hβ to obtain insight into the flare chromospheric excitation at their different formation heights. The Hα, Hβ, and Hγ lines were investigated theoretically by Kašparová et al. (2009), who used 1D radiation hydrodynamics and test particle modeling to simulate the propagation, scattering, and collisional energy loss of an electron beam (including direct collisional excitation of the hydrogen lines by beam particles), and calculate the emergent Balmer-line radiation. They demonstrated that Balmer-line intensities are expected to be correlated on sub-second timescales, and that the intensity variations in line centers and line wings are dependent on the atmospheric heating, and the parameters of the electron beams.

It must be stressed that simultaneous Hα and Hβ observations for a flare are very rare. Therefore, the results obtained from the present investigation could provide new and important insights into the comprehension of flare emission mechanisms in relevant wavelengths and atmospheric heights.

In this paper, we study the flare SOL2014-04-22, which occurred close to the western limb of the Sun, and compare observational data acquired from ground-based and satellite instruments with the results obtained from the Radiative hydrodynamic (RADYN) code (Carlsson & Stein 1997, and Allred et al. 2005, 2015) in order to investigate the behavior of Hα and Hβ, in response to the energy injected into the chromosphere during flaring. From observations and RADYN models of energy injection by an electron beam, we obtain and compare the absolute Hα and Hβ intensities, and their ratios, at high temporal resolution. We find that variations of this ratio between footpoints might be due to variations of the injected energy flux between models, suggesting that a well-calibrated Hα/Hβ ratio, and sufficiently high temporal and spatial resolutions, could provide information on flare energy injection. We also examine the observed and simulated Hα line profile; the comparison allows us to constrain the filling factor of Hα-emitting material.

We believe that this study is useful for planned future observations with the next generation of large aperture solar telescopes, such as the Daniel K. Inouye Solar Telescope (formerly the Advanced Technology Solar Telescope, Keil et al. 2010) and the European Solar Telescope (Collados et al. 2010).

This paper is organized as follows. In Section 2 we describe the observational data and in Section 3 the data analysis is reported. In Section 4 the results obtained from the RADYN models are reported and discussed. In Section 5 we draw our conclusions.

2. Observations

An observing campaign was carried out on 2014 April 22 at Dunn Solar Telescope (DST) at the US National Solar Observatory in New Mexico, using two different instruments: the Interferometric Bidimensional Spectrometer (IBIS, Cavallini 2006) and the Rapid Oscillations in the Solar Atmosphere (ROSA, Jess et al. 2010). The target of the observations was AR 12035,

67.7W 12.4S, which is characterized by a $\beta\gamma$ configuration (see Figure 1).

The aim of the campaign was to determine: (a) the source location, sizes, and eventual offset between flare sources at different wavelengths, including any offset between the Hα emission in the core and in the wings, in order to investigate whether it is possible to deduce any spatial dependence of energy deposition; (b) the time evolution of flare energy input by examining intensity variations on the shortest possible timescales; and (c) any evidence of continuum enhancement, although we do have this aim in this study.

2.1. Ground-based Observations

The IBIS instrument acquired data in two consecutive time intervals: the first data set was acquired during the pre-flare phase, while the second one covered all the C3.3 flare (flare B) evolution. More precisely, the first data set includes 1000 scans of the Hα line centered at 6563 Å from 14:22 UT to 15:05 UT; each spectral profile was sampled with a total of 17 wavelength points (average step = 0.2 Å) in about 2.61 s. The second data set consists of 900 scans of the Hα line from 15:08 UT to 15:44 UT, with the same spectral sampling used to acquire the first data set. In both cases, the Hα line was acquired in spectral mode without polarimetric measurements, with a pixel size of about 0″09 pixel^{-1}.

For each narrowband filtergram, a simultaneous broadband image (6610 ± 50 Å) was acquired, with the same exposure time and the same field of view (FOV), characterized by a circular shape, with a diameter of 90″. To reduce the seeing degradation and obtain a homogeneous resolution across the whole FOV of 1000 × 1000 pixels, the broadband images have been restored using the Multi-Object Multi-Frame Blind Deconvolution (MOMFBD, Löfdahl 2002) technique. We computed the global and local shifts necessary to align and destretch the broadband images with respect to the MOMFBD restored broadband images. The same shifts have been applied to the narrowband images.

Figure 1 (right panel) highlights the IBIS field of view with a red circle on the *SDO*/HMI continuum, while Figure 2 shows an example of the IBIS data in the continuum and in the core of the Hα line.

Co-spatial and co-temporal observations of the same active region were undertaken between 15:10:33 and 15:46:00 UT with the Rapid Oscillations in the Solar Atmosphere (ROSA; Jess et al. (2010)) imaging system installed at the DST. The data set includes simultaneous imaging in the Ca II K core at 3933.7 Å (bandpass 1.0 Å), the G band at 4305.5 Å, (bandpass 9.2 Å), continuum 4170 Å (bandpass 52.0 Å) and the Hβ core at 4861 Å (bandpass 0.1 Å), which was obtained through the universal Birefringent Filter (UBF). The G band and continuum observations were obtained with a spatial sampling of 0″069 pixel^{-1}, whereas the Ca II K and Hβ observations have a spatial sampling of 0″138 pixel^{-1}. The total field of view of ROSA images is 69″ × 69″, centered at S12.4 W67.3 in heliographic coordinates. High-order adaptive optics (Rimmele 2004) were applied throughout the observations to compensate for local seeing fluctuations.

The images were reconstructed by implementing the speckle algorithms of Wöger et al. (2008), followed by de-stretching. These algorithms have removed the effects of atmospheric distortion from the data. The effective cadence after reconstruction is reduced to about 9.238 s for Hβ, 2.3 s for Ca II K,
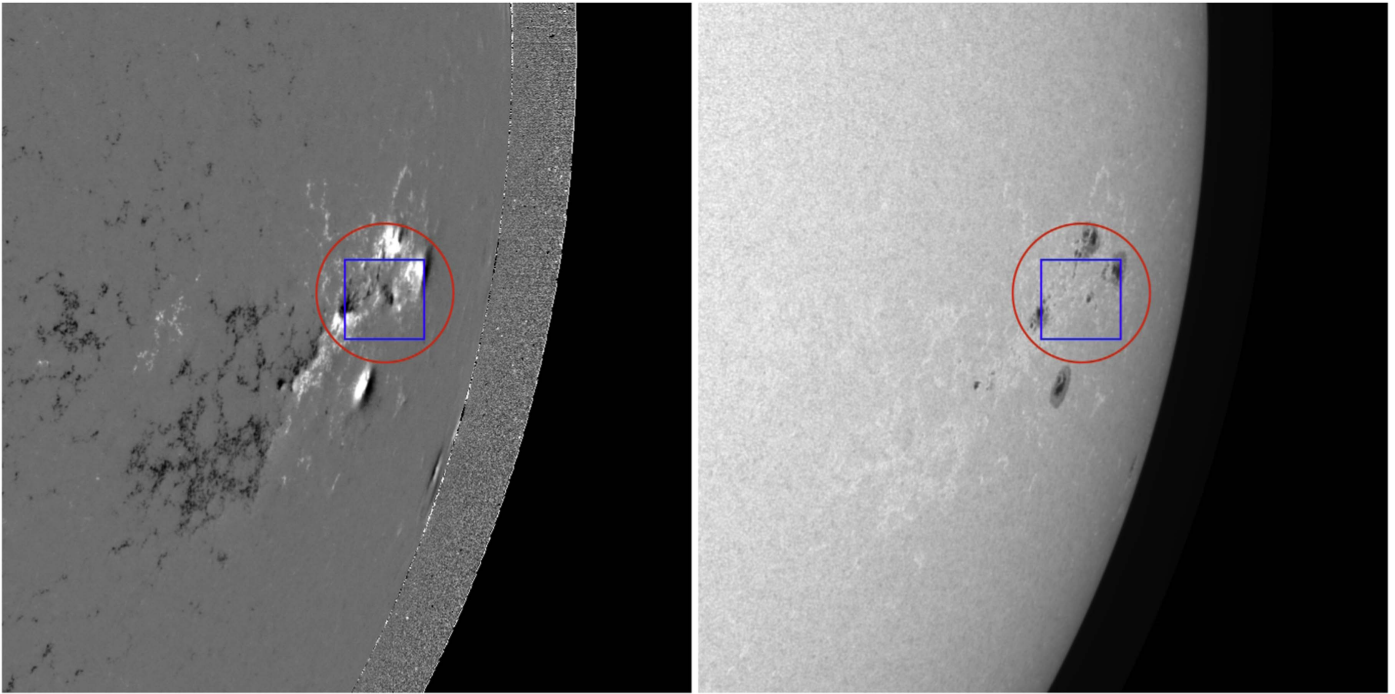
Figure 1. Left: HMI/*SDO* magnetogram showing AR 12035 on 2014 April 22. White (black) regions indicate sites of positive (negative) longitudinal magnetic field. Right: HMI/*SDO* continuum image showing the photospheric configuration of AR 12035 on the same day. The red circle, with a diameter of 90″, displays the IBIS field of view; the blue box, with a size of ~59″, indicates the ROSA field of view. In this and in the following images, if not otherwise specified, north is on top and west is to the right.

(a)   (b)
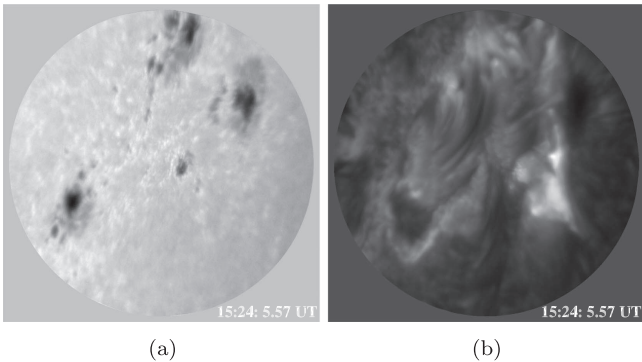
Figure 2. IBIS FOV after the flare peak: (a) continuum and (b) Hα line core.

and 2.112 s for the G band and continuum. Moreover, the FOV is reduced as a result of the Speckle reconstruction algorithm, as an apodisation windowing function is applied to the images to reduce artifacts introduced by Fourier transforms. The FOV of the reconstructed images is subsequently reduced to 58″65 × 58″65.

2.2. Space-based Observations

Context images acquired with the Helioseismic and Magnetic Imager (HMI, Scherrer et al. 2012) and the Atmospheric Imaging Assembly (AIA, Lemen et al. 2012) instruments on board the *SDO* (Pesnell et al. 2012) were used to provide general information on the magnetic field configuration and the morphology of the AR. Data from the quadrant diodes at 1–7 Å of Euv SpectroPhotometer (ESP), part of the Extreme ultraviolet Variability Experiment (EVE, Woods et al. 2012) on board *SDO*, were used to estimate the GOES classification of the flare.

In order to have information on the high energy flare emission we also used data acquired by the Reuven *Ramaty High Energy Solar Spectrometer Imager* (*RHESSI*; Lin et al. (2002)).

As described in the following section, a solar flare occurred in NOAA 12035, starting at 15:17 UT, peaking at 15:21 UT, and ending at 15:30 UT. GOES data were not available for this event; however, EVE/ESP data represent a good proxy for GOES data and allow us to classify it as a C3.3 flare (Hock et al. 2013). It is important to highlight that a few minutes before, another flare occurred at the solar limb very close to NOAA 12035. To differentiate these events, we indicate with the letter B the C3.3 flare under analysis, while the letter A indicates the flare that occurred previously.

Full-disk continuum images and longitudinal magnetograms taken by HMI in the Fe I line at 6173 Å with a resolution of 1″ were used to complement the high-resolution data set of the ground-based instruments.

The *SDO*/HMI images were aligned, taking into account the solar differential rotation,using the IDL SolarSoft package (Freeland & Handy 1998).

Data taken by AIA (Lemen et al. 2012) were used to study in detail the temporal evolution of the flare in the coronal and upper chromospheric layers. The AIA full Sun images were processed with the usual SSW `aia_prep` routines (Boerner et al. 2012, 2014). EUV and UV (1600 and 1700 Å) images have cadences of 12 and 24 s, respectively.

We reconstructed *RHESSI* CLEAN images using front detectors 3 to 8, for the energy ranges 6–9 and 12–25 keV (Hurford et al. 2002). A sequence of 6–9 keV images with an integration time of 32 s, stepping every 8 s, was constructed to obtain the light curves of flares A and B, as described in Section 3.
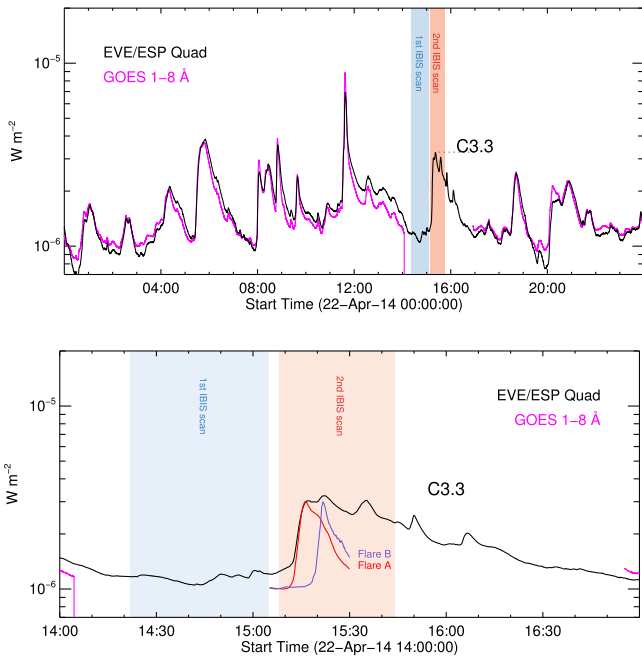
Figure 3. Upper panel: emission recorded by GOES 1–8 Å and *SDO*/EVE ESP quad detector 1–7 Å on 2014 April 22. It should be noted that between 14:10 UT and 17:00 UT, GOES data are missing. Bottom panel: enlargement of the above panel, showing the details of the emission recorded by *SDO*/EVE ESP. In both panels, the light blue and pink bands indicate the times of IBIS acquisition. The red and violet curves show the AIA 131 Å emission of flares A and B; see Figure 4.

3. Data Analysis

3.1. The Flare Evolution

The first IBIS data set (from 14:22 to 15:05 UT) shows many small brightenings in the wings of the Hα line, probably Ellerman bombs occurring in a region of magnetic flux emergence (Ellerman 1917; Kurokawa et al. 1982; Nindos & Zirin 1998). During the acquisition of the second data set (from 15:08 UT to 15:44 UT) in the southwest quadrant of the Sun, two flaring regions were observed: a limb flare (flare A) in AR 12036 (start time 15:11:34 UT, end time 15:30:22 UT, peak time 15:16 UT), and a flare event (flare B) in AR 12035 (start time 15:17 UT, end time 15:30 UT, peak time 15:21 UT).

These two flares therefore overlap in time, making it difficult to use full Sun data, like, for instance, the *RHESSI* full Sun spectral analysis or the *SDO*/EVE. However, using AIA and *RHESSI*'s imaging capabilities, it is possible to infer the contributions from each flare and retrieve some information. GOES data are not available, therefore, we used the EVE/ESP quadrant diode 1–7 Å as a proxy (see Figure 3).

We used the AIA 131 Å channel as a reference to distinguish the two flares, because this AIA channel has a temperature response close to the plasma temperatures that can be observed by *RHESSI* at low energies. We were able to image each flare independently with *RHESSI*, as shown in Figure 4. To evaluate how each flare evolves, we defined a box around the location of each flare (dotted boxes in Figure 4) and obtained the average emission in the AIA 131 Å channel (in DN s^{-1} pixel^{-1}).

In Figure 5 we show, from top to bottom: *RHESSI* counts (full Sun); AIA 131 Å emission of flares A and B along with *RHESSI* emission at 6–9 keV derived from the images; and AIA emission from each EUV and UV channel for flare B. The

Figure 4. AIA 131 Å image (reverse color) overlapped with the *RHESSI* contours in the 6–9 keV range, showing the location of flares A and B (see the text).

Figure 5. From top to bottom: *RHESSI* counts (full Sun); AIA 131 Å emission of flares A and B along with *RHESSI* emission derived from images; and AIA emission from each EUV and UV channel for flare B.
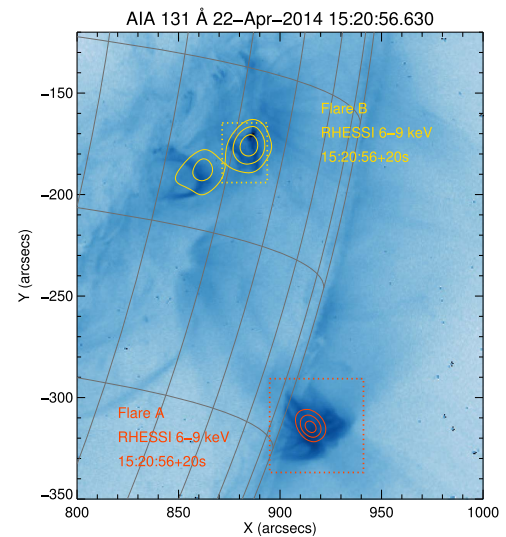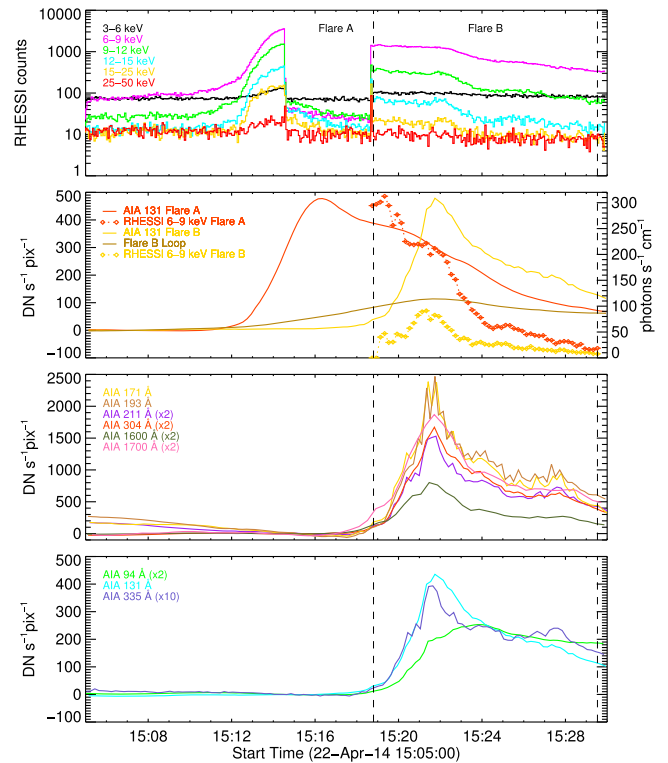
peak in the AIA 131 Å channel occurs at 15:16:20 UT and 15:21:44 UT for flares A and B, respectively. From the AIA 131 Å emission in the second panel of Figure 5 it is clear that the gradual phase of flare A extends during the impulsive phase of flare B. Therefore, we cannot use *RHESSI* full Sun spectroscopic analysis to study flare B.

The analysis of the IBIS and ROSA data set allows us to follow the flare evolution in the chromosphere, which is mainly characterized by a loop-like structure with a cusp at its top (see, e.g., the right panel of Figure 2) oriented toward the southwest.
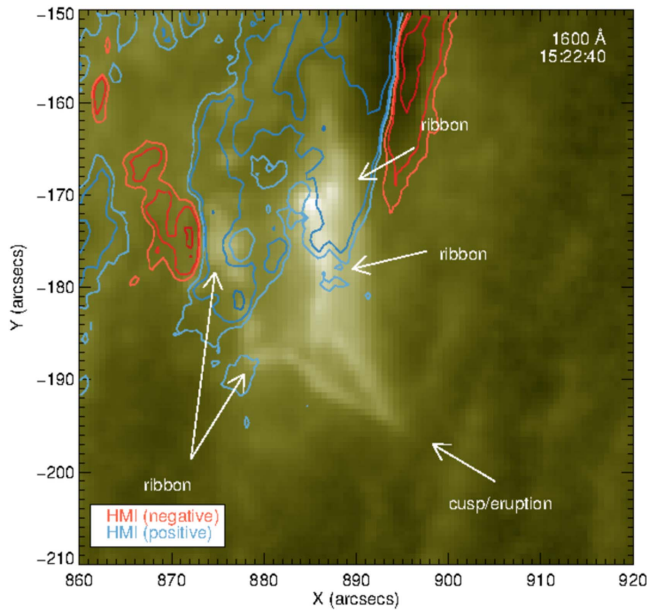
Figure 6. AIA 1600 Å image acquired at 15:22:40 UT overlapped with the HMI line-of-sight magnetic field (red: negative field, -2000, -1000, -500, -200, -100 G; blue: positive field, 100, 200, 500, 1000, 2000 G).

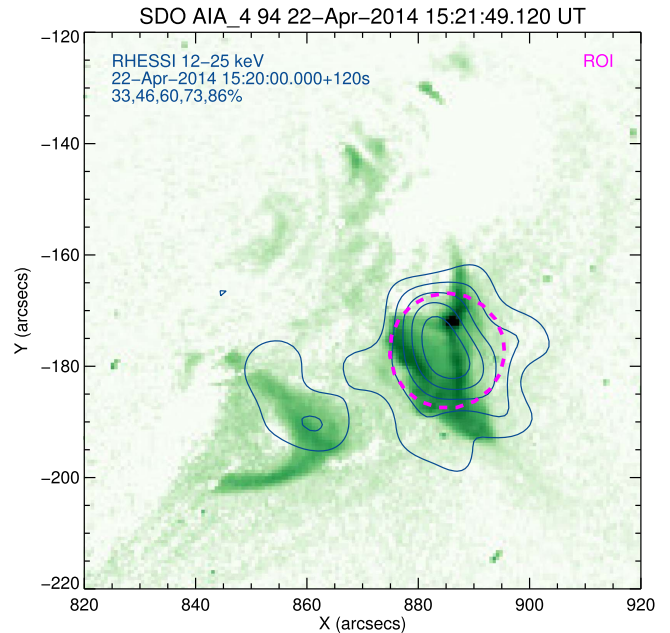**Figure 7.** AIA 94 Å image (reverse color) overlapped with the *RHESSI* emission contours in the 12–25 keV range. The purple dashed circle indicates the region of interest (ROI).

The distance between the two footpoints, as determined from the IBIS Hα image acquired at 15:24 UT (see Figure 2 right panel), is 11,500 km, and assuming a semi-circular shape for the loop-like structure, this has a length of ∼18,000 km.

Comparing with continuum images (see Figure 2, left panel), it is possible to establish that the flare developed between the large (western) sunspot and a small pore located at the center of the FOV. The large arch filament system (AFS) connecting the other two main sunspots does not seem to show any variation during the flare.

In Figure 6 we show an AIA 1600 Å image acquired at the peak of the flare, with the overlapped contours (levels indicated in the figure caption) denoting the longitudinal magnetic field deduced from the HMI instrument. Note that the cusp region, also observed at 6563 Å (compare with Figure 2, right panel), is quite evident, while the bright footpoints seem to be both located in regions of positive magnetic field, which is due to projection effects due to the proximity of the AR to the western limb.

The comparison between the AIA 94 Å image acquired ∼1 minute before the flare peak (see Figure 7) and the *RHESSI* 12–25 keV contours indicate that there are two main sources of hard X-ray emission: the location of one corresponds to the flaring loop-like structure, and the other is superimposed on another bright structure to the east of the flaring loop. It is worth noting that this feature was not in the IBIS and ROSA FOVs.

3.2. Hα–Hβ Comparison

We further investigate the flare event through the comparison between Hα and Hβ images acquired by IBIS and ROSA, respectively. In fact, although this event is not very energetic and it is very close to the limb, the combined data set is unique because it has both Hα and Hβ imaging.

Due to the fact that the images obtained by the two instruments have different sizes and spatial resolution, we first need to align the Hα and Hβ images. To this aim, we use the

USAF target images and dot grid images (see, e.g., Kleint 2012), because the sample is the same during the observing campaign, and furthermore, they were simultaneously acquired in the two channels. Through them it was possible to calculate the parameters to rotate, rescale, and shift the images in order to obtain the correct alignment between Hα and Hβ images. Once obtained, these parameters were been applied to the IBIS data set, i.e., the Hα images. Figure 8 shows the result of the alignment procedure: the images have the same orientation, size (456×478 pixels) and spatial sampling ($0\rlap{.}''138$ pixel^{-1}).

After the alignment we compared the light curves of these two chromospheric lines in four boxes inside the field of view indicated in Figures 8 ((b) and (c) panels). Three of these boxes (A, B, and C) are on the bright areas of the flare, while the last one (box D) is on a bright patch outside the flaring region. The boxes have the same size, i.e., 40×40 pixels ($\approx 5\rlap{.}''5 \times 5\rlap{.}''5$). We choose a box of this size to avoid losing information during the flare brightness evolution. We note that the locations of the flare emission inside the boxes are not fixed in space but they moved during the evolution of the event. We obtained the light curves of Hα and Hβ by taking the average intensity values calculated over all the pixels inside each box. Moreover, to better compare the intensities acquired with the IBIS and ROSA instruments, we calibrated the intensity obtained by the different cameras from DN to erg s^{-1} cm^{-2} Å^{-1} sr^{-1} units as follows: we determined the flat-field image intensity acquired on the day of observation with both the IBIS and ROSA cameras, and assuming that this flat-field intensity was equal to the values provided in the Brault & Neckel Atlas (Brault & Neckel 1987), we converted the measured intensity in DN to fundamental units. We reiterate here that the cadences for the reduced Hα and Hβ data sets are around 2.6 s and 9.2 s, respectively.

Figure 9 shows the intensity as a function of time deduced from Hα (black) and Hβ (orange) images for the four boxes. In particular, the intensity relative to the Hα line has been
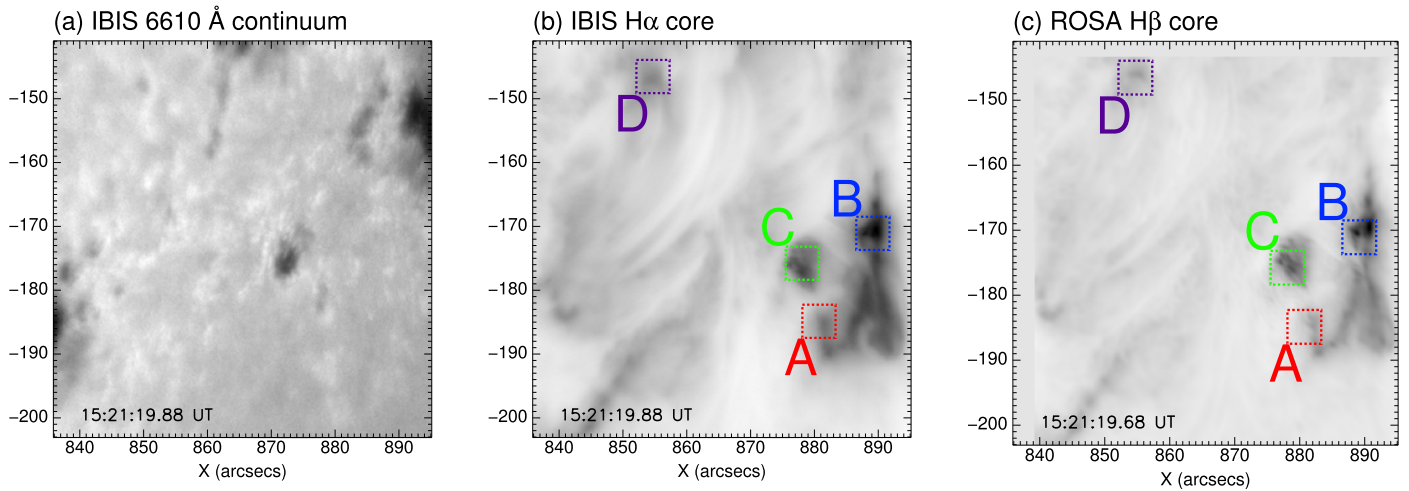
Figure 8. (a) Image acquired in the IBIS continuum at 6610 Å; (b) IBIS Hα image of the same FOV (reversed color); (c) ROSA Hβ image (inverted color) after the alignment procedure with the IBIS corresponding image. The boxes in (b) and (c) indicate the regions A, B, C, and D that are used to determine the intensity evolution (see Figures 9 and 10).

determined by averaging the intensity at the center of the line (6562.8 Å) and in an adjacent point along the line profile (6562.9 Å) covering a total $\Delta\lambda = 0.1$ Å, comparable to the bandwidth of the Hβ filter employed with the ROSA instrument. However, because the cadence of Hα images was higher than Hβ data, the sampling to determine the Hα intensity was greater. To highlight the energy released during the flare, the intensities of all the light curves were obtained by subtracting the pre-flare intensity calculated by averaging the intensity in each box during 2 minutes in a time interval before the flare, i.e., from 15:10:00 UT to 15:12:00 UT.

Analysis of these plots indicates that the intensity excess of the Hβ line is generally higher than the Hα intensity during the impulsive phase of the flare; in particular, the former can reach values up to $\sim 0.3 \times 10^6$ (box A), $\sim 1.8 \times 10^6$ (box B), and $\sim 1.1 \times 10^6$ (box C) erg s^{-1} cm^{-2} Å^{-1} sr^{-1}, while the latter reaches values of $\sim 0.2 \times 10^6$ (box A), $\sim 0.7 \times 10^6$ (box B), and $\sim 0.5 \times 10^6$ (box C) erg s^{-1} cm^{-2} Å^{-1} sr^{-1} (see the first three panels of Figure 9). The light curves obtained in box D appear flat for both the lines during all time of analysis (see the bottom panel of Figure 9). In the same plot, the vertical black lines show the estimated start (dashed) and peak (solid) flare times deduced by EVE/ESP.

The ratio of the two core spectra intensities has potential diagnostic importance for the comprehension of chromospheric flares (Kašparová et al. 2009). In order to detect any possible signature of different emission among the two wavelengths, we calculated the ratio between the Hα and the Hβ intensity for all the boxes in which we applied an 11-point smoothing function in order to remove the excess noise. The ratio values have been calculated with the common acquisition time of the two instruments, namely from 15:10 UT to 15:45 UT. The bottom panel in Figure 10 presents the temporal evolution of this ratio, where the different colors indicate the intensity ratio obtained for each box (see the legend). In the same figure, the intensities of the Hα (top panel) and Hβ (middle panel) lines are reported as a function of time for each box. Figure 10 shows that the two chromospheric lines respond to the flare energy input in the same way, highlighting a similar shift between peaks in intensity and an energy distribution comparable to the corresponding box. Specifically, the Hα light curves of boxes A, B, and C have similar behavior, with a similar peak in

intensity and similar decay phases. Similar behavior, albeit with different values of intensity, is seen in the corresponding Hβ light curves.

The bottom panel in Figure 10 shows that the Hα/Hβ intensity ratios during the flare tend to a constant value for the boxes inside the flaring region (approximately around 0.4 for boxes B and C and around 0.8 for box A), while before and after the flare, the values are generally higher, with a variable trend for all the boxes. Outside the flaring region (box D) the ratio is highly unstable, with large oscillations before, during, and after the energy input, due to the low values of the intensity that cause large errors.

3.3. Spatial Offset

Following the aim of the observing campaign, to evidence a possible spatial offset among each chromospheric sources, we looked at the maximum intensity value inside the corresponding box (note, it is possible that this location will not occur exactly in the same pixels for both Hα and Hβ channels). In Figure 11 we report the spatial offset as a function of time between the brightest points in the Hα and Hβ line cores for boxes A and B and the offset between the brightest points in the Hα core and Hα continuum wing. We display the results only for boxes A and B because they are more relevant as they are located in the footpoints of the flare loop. The analysis of this plot shows a spatial offset in the range of 2″–3″ between the sources imaged in the Hα and Hβ line cores, but in box A this offset decreases to 0″.2 after the impulsive phase of the flare, while remaining constant for box B. The distance between the brightest points observed in the Hα core and Hα wing is constant for box A, around a value of 3″, while it varies from 1″–5″ for box B.

3.4. Evolution of the Hα Line Profile

In order to investigate the temporal evolution of the Hα line profile and to compare it with the simulations shown in Section 4, we selected a time interval of 10 minutes during the flare evolution, starting at 15:15:50 UT, and calculated the average intensity at each point of the line acquired by IBIS (it should be noted that a similar analysis for the ROSA Hβ data set could not be performed because in this case we only have images in
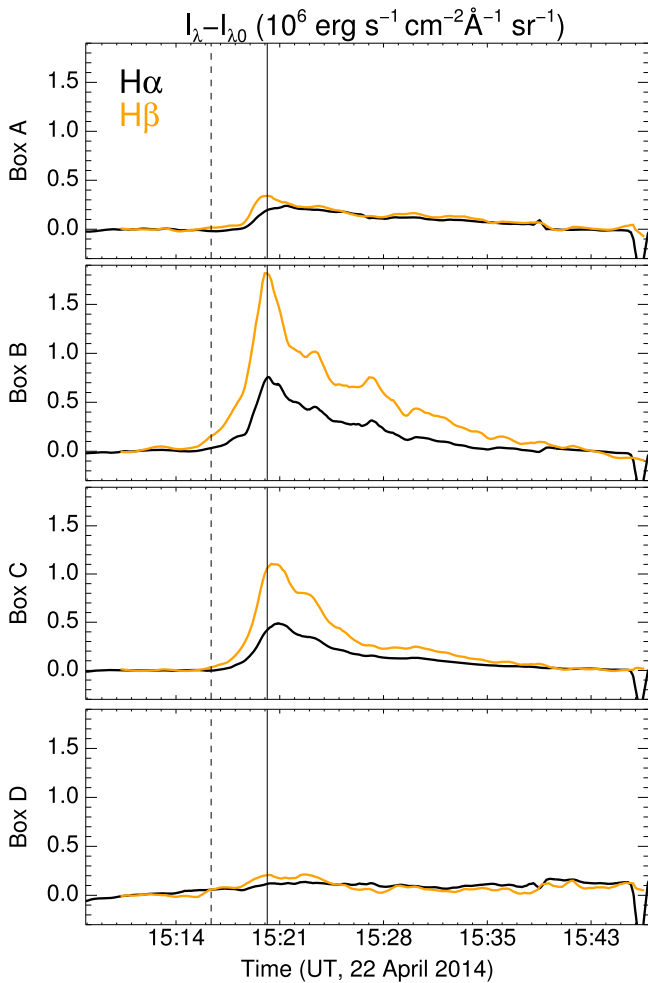
Figure 9. Average intensity (after subtraction of the pre-flare intensity; see the text) as a function of time deduced from Hα (black) and Hβ (orange) data in the three boxes located within the flare location (A, B, and C) and in a box outside the flaring region (D). The vertical black lines show the estimated start (dashed) and peak (solid) times of the flare. The co-temporal drops at the end of the sequence are related to the bad seeing conditions.

the line center). Again, this analysis was only carried out for boxes A and B.

Figure 12 (left panel) shows that in box A the Hα line shows a stronger increase in the red wing, compared to the blue wing, and that the line core is shifted blueward. In box B, the line exhibits both red and blue wing enhancements (see Figure 12, right panel). The core is more enhanced than in box A but it does not go into emission. In box B the core shows a very small redshift during the rise phase (up to 200 s, see Figure 12, right panel), shifting to shorter wavelengths afterward. In both boxes A and B, the line does not show a central reversal. Deng et al. (2013) reported similar observations, in contrast to typical observations of the Hα line profile (Canfield et al. 1990; de La Beaujardiere et al. 1992; Kuridze et al. 2015).

4. RADYN Simulations

We used the radiative hydrodynamic code RADYN to compute the Hα and Hβ line profiles and to calculate the intensity ratio of the line cores for comparison with the observations. Our idea is to adopt the model closest to the observation features, using the *RHESSI* imaging spectroscopy integrated over 2 minutes during the main impulsive phase
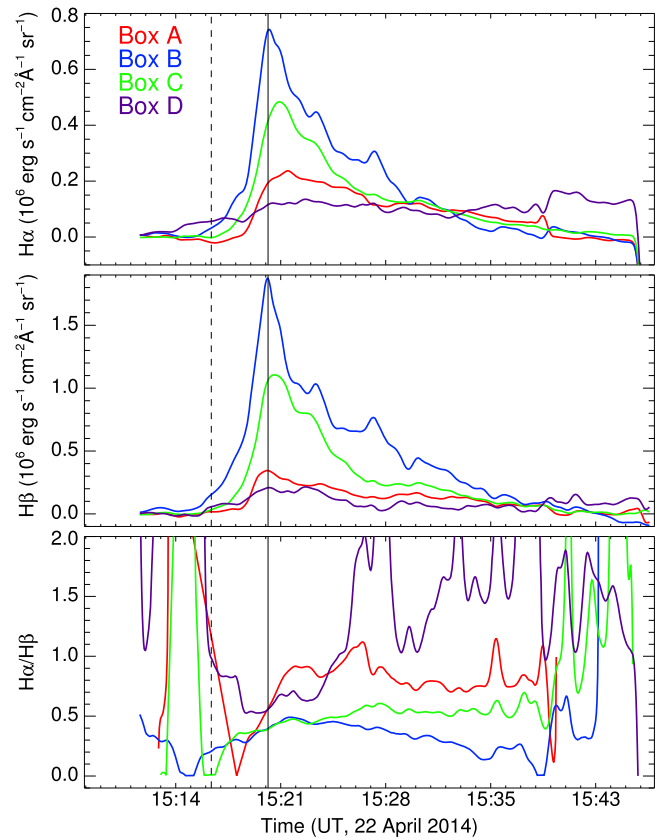

Figure 10. Temporal evolution of the Hα excess intensity (top panel) and the Hβ excess intensities (middle panel) in boxes A, B, C, and D indicated in Figure 8 (b)–(c). The bottom panel shows the temporal evolution of the ratio Hα/Hβ. Different colors indicate different boxes (see the legend in the plot). The vertical black lines show the estimated start (dashed) and peak (solid) flare times.
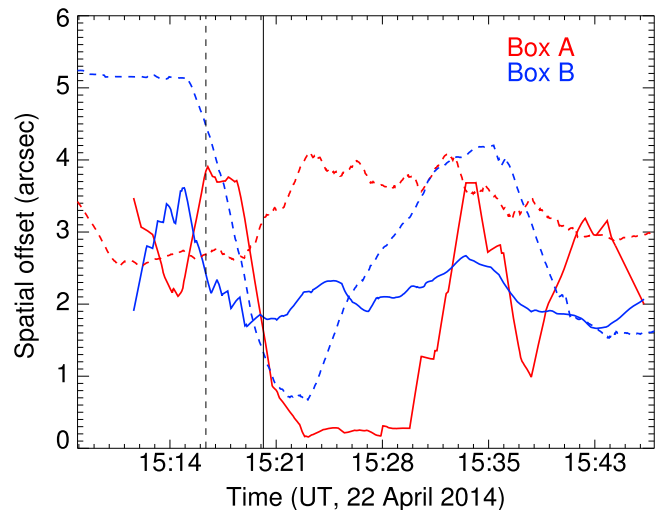

Figure 11. Temporal evolution of the offset of the brightest points imaged in the Hα and Hβ line cores inside boxes A and B (solid lines). The dashed lines indicate the same, but for the Hα core line and Hα wing.

(15:20:00–15:22:00 UT). Figure 13 shows *RHESSI* photon spectra for the hard X-ray source spatially integrated over the ROI displayed in Figure 7. The spectra were fitted with an isothermal-plus-thick-target model, shown in Figure 13 with the orange line, and the resulting parameters are: emission
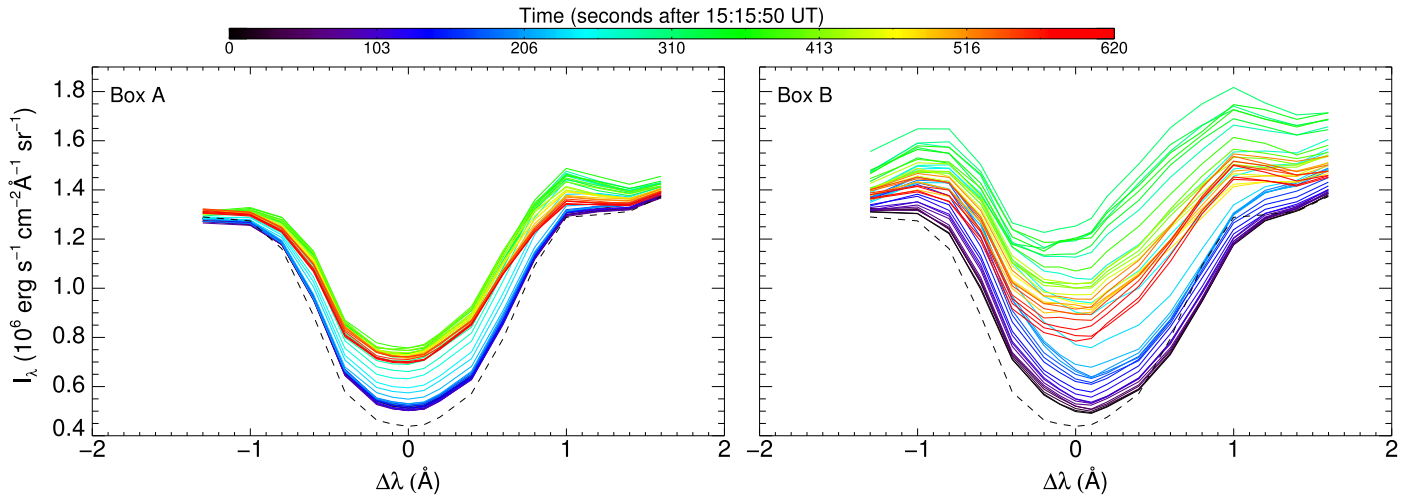
Figure 12. Temporal evolution of the observed Hα profile in box A (left) and box B (right). The intensities are reported in absolute units. Different colors indicate different times (from black, through blue, and green to dark red). The dashed profile results from the average intensity in each box at the beginning of the observing sequence.
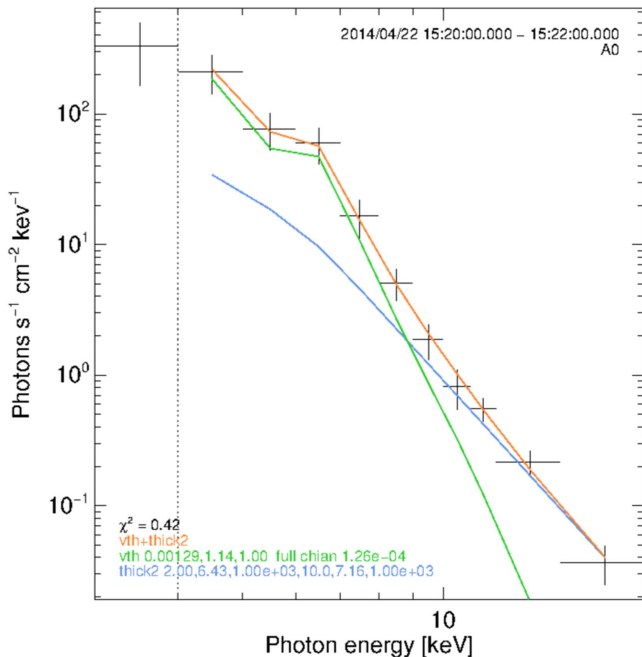

Figure 13. *RHESSI* photon spectra for the hard X-ray source over the ROI indicated by the purple dashed circle in Figure 7 and integrated for the interval 15:20:00–15:22:00 UT. The orange line is the isothermal-plus-thick-target model. The isothermal model is the green line, defined by two parameters: emission measure EM and temperature T (see the text). The non-thermal thick-target model is the blue line, defined by three parameters: low energy cutoff E_c, spectral index δ, and total number of electrons per second above E_c.

measure EM $= 1.3 \times 10^{46}$ cm^{-3}; plasma temperature $T = 13$ MK; number of electrons per second injected $F = 2 \times 10^{35}$ electrons s^{-1} above $E = E_c = 7$ keV; spectral index $\delta = 6.4$; total non-thermal power $P_{nth} = 2.7 \times 10^{27}$ erg s^{-1}; and total non-thermal energy $E_{nth}^{tot} = 3 \times 10^{29}$ erg. From these parameters, two RADYN simulations were employed here, the first one, marked by F9.5, with a peak of energy flux of $F_{F9.5}^{max} = 3 \times 10^9$ erg cm^{-2} s^{-1} and a total amount of energy $F_{F9.5}^{tot} = 0.3 \times 10^{11}$ erg cm^{-2}; and the second one, indicated by F10, with a peak of $F_{F10}^{max} = 10^{10}$ erg cm^{-2} s^{-1} and a total amount of energy $F_{F10}^{tot} = 10^{11}$ erg cm^{-2}. For both the runs a

beam with an isotropic pitch angle distribution in the forward hemisphere was used with the Fokker–Planck solution to the non-thermal electron distribution (Allred et al. 2015). A triangular, pulse-shaped heating flux was applied for 20 s (with a peak after 10 s), and the atmosphere was allowed to relax for 15 additional seconds. The initial atmosphere before the switch-on of the beam was the VAL3C semi-empirical atmosphere (Vernazza et al. 1981). The electron-beam energy distribution is defined as a power-law with a spectral index of $\delta = 6$ and a low energy cutoff $E_c = 10$ keV. Considering the location of the flare on the solar disk, to simulate the projection effect we used $\mu = 0.23$ in both F9.5 and F10 runs.

Using the Hα and Hβ lines profiles calculated with RADYN, we computed the ratio of the line core intensities, $\lambda = 6563$ Å for Hα and $\lambda = 4861$ Å for Hβ, for both models F9.5 and F10, the results of which are shown in Figure 14. In both models, for the duration of the energy input, the ratio of Hα to Hβ is smaller than 1. In F10 the ratio starts around 0.6–0.7, then settles at 0.4 after 10 s, very similar to the observed ratios of boxes B and C. In F9.5 the ratio swings between 0.6–0.8, closer to the observed ratios of box A, which is the weakest flare kernel.

Figure 15 shows the temporal evolution of the synthesized Hα line profile for both the F10 and F9.5 flare models. In the F9.5 model, the line, initially in absorption, goes into emission with a clear presence of a central reversal. Through the duration of the energy input, the line wings around $\Delta\lambda \approx -0.5$ are much more pronounced than the line core. During the first 15 s of the energy input, the entire line profile is shifted toward longer wavelengths, with the blue wing being stronger than the red wing. From then until the end of the energy input at $t = 20$ s, the line shifts slightly redward from the rest wavelength and the wings are more symmetric. When the energy input stops, the intensity of the wings and core decreases substantially, a red-wing asymmetry appears, and the core is shifted $\Delta\lambda > 0$.

In the F10 model, the line also goes into emission with a central reversal, with a much more pronounced intensity of the line core with respect to the wing intensities, compared to the F9.5 model. As noted by Kuridze et al. (2015), a red wing asymmetry (i.e., the red wing intensity stronger than the blue wing) develops in the first 5 s, before reverting to a blue wing
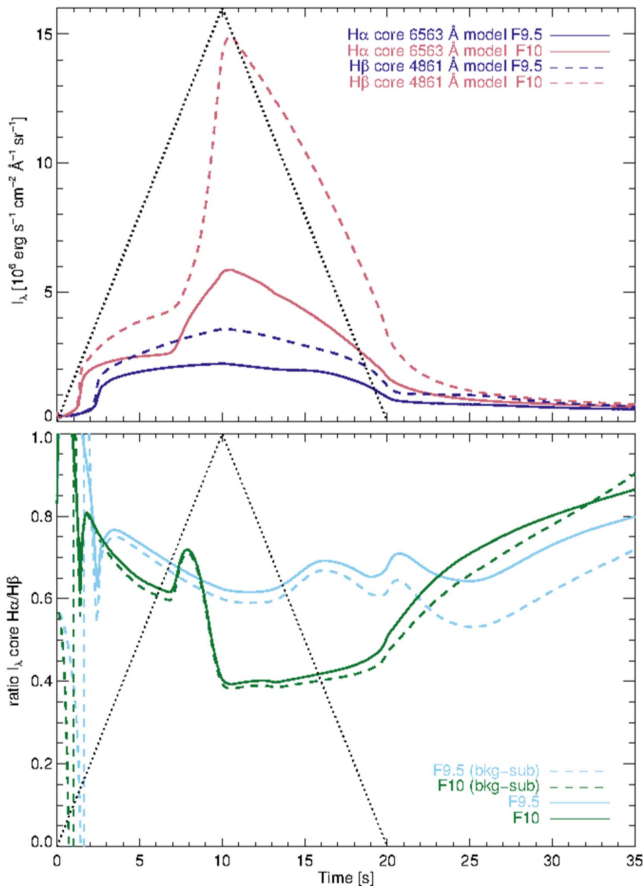
Figure 14. Time evolution of the intensity and the ratio of the core in the Hα and Hβ lines, for the F9.5 and F10 models (see the legend). The black dotted lines show the shape of the energy input.

Figure 15. Time evolution of the Hα line profile calculated with RADYN, for the F9.5 (top) and F10 (bottom) flare models.

asymmetry after that time. The line core shifts to opposite directions: blueward and then redward. The wing asymmetry is created by an excess of absorption by the moving plasma above the height of formation of the Hα line, as pointed out by Kuridze et al. (2015), i.e., a red asymmetry does not necessarily indicate the presence of downward moving plasma, nor does a blue asymmetry indicate upwardly moving plasma. When the energy input ends, the line intensity drops rapidly, and the wings become much less pronounced (even disappearing), but the line remains in emission until the end of the simulation.

The synthetic Hα line profiles obtained from the RADYN simulations are different from the profiles observed with IBIS, as described earlier. The line profiles in both boxes A and B remain mostly in absorption throughout the event, with a stronger increase in the core intensity than in the wing intensities.

It is possible that not all the pixels inside the box are activated by the flares, so the "filling factor", defined as $ff = 1/(N + 1)$, is smaller than 1. We have tried to simulate this filling factor effect with the RADYN lines by averaging N times the pre-flare line profile with the flaring lines, namely $I_{ff} = ff\,(I_{flare} + NI_{pre-flare})$. In practical terms, this brings the calculated lines closer to the observed line shape. For both the F9.5 and F10 models, we found solutions that qualitatively reproduce the observations: $N_{F9.5} = 2$ and $N_{F10} = 5$, with filling factor values $ff_{F9.5} = 0.333$ and $ff_{F10} = 0.167$. Figure 16 shows the line profiles using that filling factor. The plots show that the line is in absorption, prior to a small enhancement of
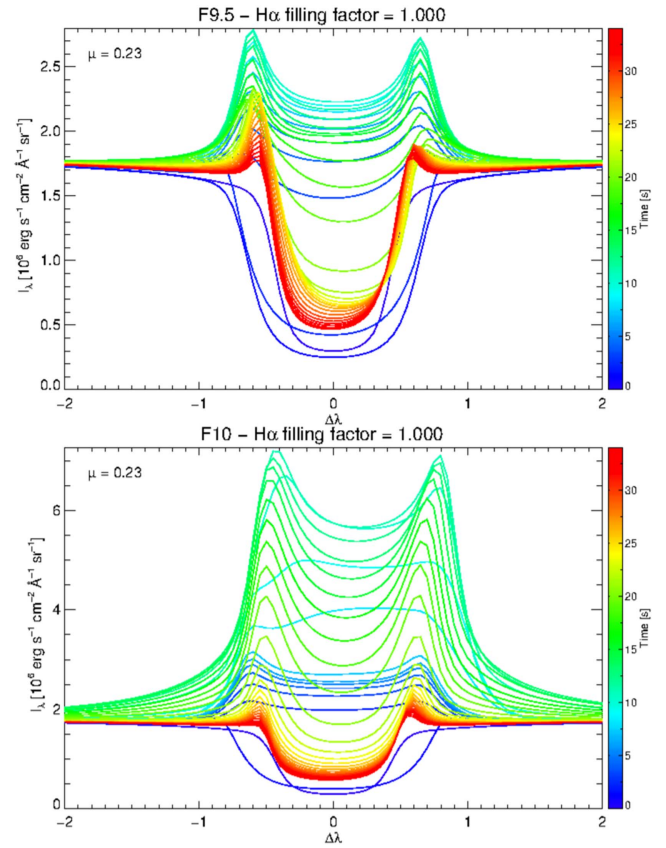
the wings around $\Delta\lambda \pm 1.0$ Å. In F10 there is a small enhancement at $\Delta\lambda \pm 1.0$ Å, and in F9.5 the blueshift of the line core follows the observations closer than that of F10. In absolute values of I_λ, F10 gives a better agreement in $I(\Delta\lambda = 0)$, with F9.5 being too weak.

Note that with Hβ we do not have line scans as we do with Hα. The Hβ images are from the core of the line, and have a relatively broad filter width in comparison to the Hα scans. Therefore, the RADYN simulation cannot be used for a direct comparison for the Hβ images.

We used the F9.5 and F10 models to qualitatively explore a weak and a strong case. To determine which of the two runs is closer to observations we have to derive the total amount of energy injected in the two models. RADYN solves equations along one dimension, but the observation results are related to boxes of two dimensions. Our idea is to translate the filling factor discussion in an area value in order to obtain a size for the flaring elements. Comparing the observed and synthetic Hα line profiles (see Figure 12 and 14), we obtained a different value of filling factor from F9.5 and F10 runs. Knowing the size of the box used in the observations (5″5 × 5″5), we can easily convert them to a simulated flaring area: ≈3″2 × 3″2 for F9.5 and ≈2″2 × 2″2 for F10. To estimate the projection effect, from the location of the flare source on the solar disk we obtained $\mu = 0.3$, and using this value, the effective flaring areas are then $A_{F9.5}^{eff} = 17.5 \times 10^{16}$ cm² and $A_{F10}^{eff} = 8.8 \times 10^{16}$ cm². From the *RHESSI* photon spectra fit parameters and using the effective flaring areas, we found $F = P_{nth}/A_{F9.5}^{eff} \approx 0.15 \times 10^{11}$ erg s⁻¹ cm⁻² and $F = P_{nth}/A_{F10}^{eff} \approx 0.31 \times 10^{11}$ erg s⁻¹ cm⁻². The real problem here is
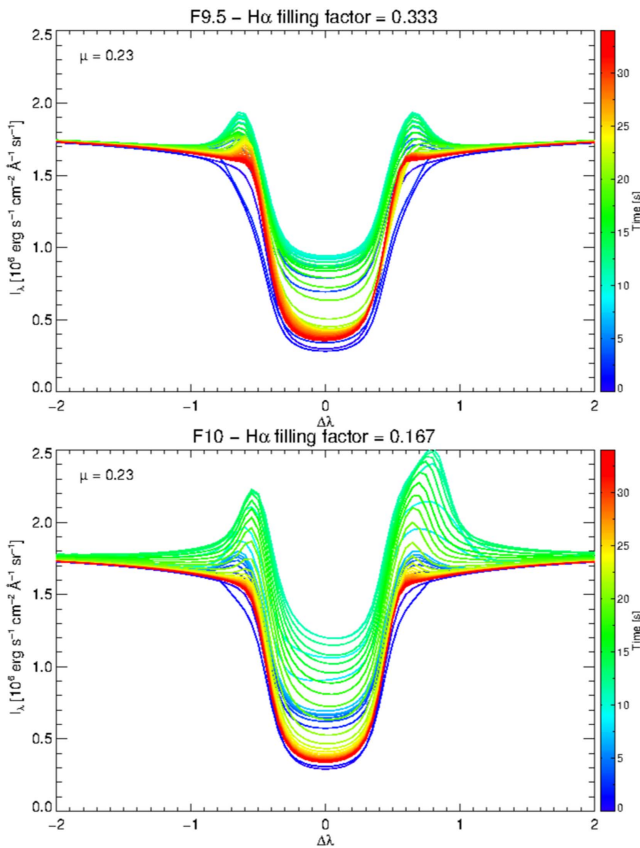
Figure 16. Same as Figure 15, but simulating a filling factor *ff* smaller than 1 (see the text). Top: F9.5 model, *ff* = 0.167. Bottom: F10 model, *ff* = 0.048.

that the *RHESSI* values are derived from the whole flare (see the ROI in Figure 7), not just one source (box), but the F9.5 model appears closer to the observations.

5. Conclusions

The aim of this work was to clarify some aspects related to energy release and redistribution in the chromospheric layer of the solar atmosphere during a solar flare. Therefore, we investigated the chromospheric response to the sudden energy input, locating the sources, the sizes, and the eventual offset between flare sources in different wavelengths. Our approach was to look at the features of two chromospheric lines during a C3.3 solar flare, using high-resolution ground-based data acquired during an observing campaign carried out at Dunn Solar Telescope. Although the location of the flare on disk was not ideal and the intensity of the event was relatively low, the uniqueness of this data set in terms of the resolution (both spatial and temporal), the lines used (both Hα scans and Hβ core images) and the fact that all phases of the flare were observed, provides novel insights into the behavior of the chromosphere during a flare.

In a previous work, Kašparová et al. (2009) simulated Balmer lines during impulsive flare heating and investigated the correlation between Hα and Hβ lines. The authors tried to use the Hα/Hβ ratio to check whether they are sensitive to electron-beam presence, i.e., whether they are significantly different if the non-thermal collisional rates are included in the simulations. In this paper we displayed the light curves from observed Hα and Hβ lines, where, in the flaring region, the Hβ

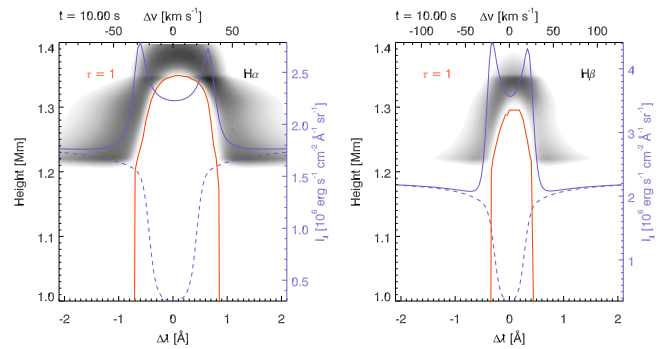**Figure 17.** Intensity contribution functions for the Hα (left) and Hβ (right) lines after 10 s of F9.5 flare heating. The diagrams are plotted in inverse grayscale so that darker shades indicate higher intensities. The line profile is overplotted as a blue line. The red lines indicate the height at which $\tau = 1$. Positive velocity corresponds to plasma upflows.

intensity excess is greater than those of Hα during the flare energy input, as noted by Kašparová et al. (2009).

We employed the radiative hydrodynamic code RADYN to compute the synthetic Hα and Hβ line profiles to compare them with our observations. For both the F9.5 and F10 runs the Hβ intensity is greater than Hα, while the intensity ratio is around 0.4 in the F10 model after the energy peak, which is in agreement with the observed ratios for the different regions of the flare. Similar ratios from different inputs implies that the Hα and Hβ lines are affected similarly by the amount of energy, and this indicates that this ratio is sensitive to the amount of energy deposited in the chromosphere.

Our results for the line ratios are in agreement with the findings of Kašparová et al. (2009). In Kašparová et al. (2009), Flarix gives intensities in erg s^{-1} cm^{-2} Hz^{-1} sr^{-1} and also line ratios are computed from those values, while in this paper we used erg s^{-1} cm^{-2} Å^{-1} sr^{-1} as I_λ units. As confirmed by private communication with the authors, the ratio should be around 0.5 after adjusting to the same units of I_λ used in this paper, which is very close to our results.

Furthermore, by comparing the observed and synthetic Hα line profile evolutions, there is good agreement using a "filling factor" approach. The simulated Hα profiles present a clear central reversal, while the observed line profiles were enhanced during the flare, but remained mostly in absorption. We have interpreted the weakly enhanced Hα line profiles as an effect of a low filling factor, estimated to be *ff* ≈ 0.33 or *ff* ≈ 0.17, using models F9.5 and F10, respectively. The simulated intensity ratios, with the pre-flare level subtracted, yield, for the low filling factor cases, values of 0.4–0.5. This is simply because the same filling factor was applied for both the Hα and Hβ line profiles. Furthermore, converting the filling factor in terms of flaring area, we obtained values of total energies for the F9.5 and F10 models, indicating the F9.5 closer to the observations.

Concerning the analysis related to the spatial offset, because the flare is located close to the limb, we can read the results as diagnostic of the formation heights of the two line cores. Figure 17 displays the line contribution functions (Carlsson & Stein 1997) after 10 s of F9.5 flare input, where the Hα core formation height is higher than about 40 km with respect to the Hβ core (wings formation heights are the same). The observed spatial separation is in qualitative agreement with the RADYN simulation, and the observed spatial offset is much larger, but this may be due to one-dimensional limit of RADYN code, so

it is hard to make an actual comparison with imaging observations. Therefore, a possible suggestion for future observations in both spectral lines would be to search for flaring active regions very close to the solar limb, in order to further investigate the spatial offset.

ORCID iDs

Francesca Zuccarello ⬤ https://orcid.org/0000-0003-1853-2550
Paolo Romano ⬤ https://orcid.org/0000-0001-7066-6674
David Kuridze ⬤ https://orcid.org/0000-0003-2760-2311
Mihalis Mathioudakis ⬤ https://orcid.org/0000-0002-7725-6296
Gianna Cauzzi ⬤ https://orcid.org/0000-0002-6116-7301
Mats Carlsson ⬤ https://orcid.org/0000-0001-9218-3139

References

Abbett, W. P., & Hawley, S. L. 1999, ApJ, 521, 906
Allred, J. C., Hawley, S. L., Abbett, W. P., & Carlsson, M. 2005, ApJ, 630, 573
Allred, J. C., Kowalski, A. F., & Carlsson, M. 2015, ApJ, 809, 104
Boerner, P., Edwards, C., & Lemen, J. 2012, SoPh, 275, 41
Boerner, P. F., Testa, P., Warren, H., Weber, M. A., & Schrijver, C. J. 2014, SoPh, 289, 2377
Brault, J., & Neckel, H. 1987, Spectral Atlas of Solar Absolute Disk-Averaged and Disk-Center Intensity from 3290 to 12510 Å (Hamburg: Hamb. Sternw.)
Canfield, R. C., Gunkler, T. A., & Ricchiazzi, P. J. 1984, ApJ, 282, 296
Canfield, R. C., Penn, M. J., Wulser, J., & Kiplinger, A. L. 1990, ApJ, 363, 318
Carlsson, M., & Stein, R. F. 1997, ApJ, 481, 500
Carmichael, H. 1964, in Proc. of the AAS-NASA Symp., The Physics of Solar Flares, ed. Wilmot N. Hess (Washington, DC: NASA), 451
Cavallini, F. 2006, SoPh, 236, 415
Collados, M., Bettonvil, F., Cavaller, L., et al. 2010, AN, 331, 615
de La Beaujardiere, J. F., Kiplinger, A. L., & Canfield, R. C. 1992, ApJ, 401, 761
Deng, N., Tritschler, A., Jing, J., et al. 2013, ApJ, 769, 112
Ellerman, F. 1917, ApJ, 46, 298
Fletcher, L., Dennis, B. R., & Hudson, H. S. 2011, SSRv, 159, 19
Freeland, S. L., & Handy, B. N. 1998, SoPh, 182, 497
Hirayama, T. 1974, SoPh, 34, 323
Hock, R. A., Woodraska, D., & Woods, T. N. 2013, SpWea, 11, 262
Hurford, G. J., Schmahl, E. J., & Schwartz, R. A. 2002, SoPh, 210, 61
Jess, D. B., Mathioudakis, M., Christian, D. J., et al. 2010, SoPh, 261, 363
Kašparová, J., Varady, M., Heinzel, P., Karlický, M., & Moravec, Z. 2009, A&A, 499, 923
Keil, S. L., Rimmele, T. R., Wagner, J. & ATST Team 2010, AN, 331, 609
Kleint, L. 2012, ApJ, 748, 138
Kopp, R. A., & Pneuman, G. W. 1976, SoPh, 50, 85
Kuridze, D., Mathioudakis, M., Simões, P. J. A., et al. 2015, ApJ, 813, 125
Kurokawa, H., Kawaguchi, I., Funakoshi, Y., & Nakai, Y. 1982, SoPh, 79, 77
Lemen, J. R., Title, A. M., Akin, D. J., et al. 2012, SoPh, 275, 17
Lin, R. P., Dennis, B. R., Hurford, G. J., et al. 2002, SoPh, 210, 3
Löfdahl, M. G. 2002, Proc. SPIE, 4792, 146
Nindos, A., & Zirin, H. 1998, SoPh, 182, 381
Pesnell, W. D., Thompson, B. J., & Chamberlin, P. C. 2012, SoPh, 275, 3
Rimmele, T. R. 2004, ApJ, 604, 906
Scherrer, P. H., Schou, J., Bush, R. I., et al. 2012, SoPh, 275, 207
Sturrock, P. A. 1966, Natur, 211, 695
Vernazza, J. E., Avrett, E. H., & Loeser, R. 1981, ApJS, 45, 635
Wöger, F., von der Lühe, O., & Reardon, K. 2008, A&A, 488, 375
Woods, T. N., Eparvier, F. G., Hock, R., et al. 2012, SoPh, 275, 115